Dalton Transactions

High entropy effect on thermoelectric properties of nonequilibrium cubic phase of AgBiSe2−2xSxTex with x = 0–0.6

Journal:	*Dalton Transactions*
Manuscript ID	DT-ART-05-2024-001317.R1
Article Type:	Paper
Date Submitted by the Author:	20-Jul-2024
Complete List of Authors:	Seshita, Asato; Tokyo Metropolitan University - Minamiosawa Campus, Physics Yamashita, Aichi; Tokyo Metropolitan University - Minamiosawa Campus, Physics Katase, Takayoshi; Tokyo Institute of Technology - Suzukakedai Campus mizuguchi, yoshikazu; Tokyo Metropolitan University - Minamiosawa Campus, Physics

High entropy effect on thermoelectric properties of nonequilibrium cubic phase of $AgBiSe_{2-2x}S_xTe_x$ with $x = 0–0.6$

Asato Seshita,[a] Aichi Yamashita,[a,*] Takayoshi Katase,[b] Yoshikazu Mizuguchi[a]

[a] *Department of Physics, Tokyo Metropolitan University, 1-1 Minami-Osawa, Hachioji-shi, Tokyo 192-0397, Japan*

[b] *MDX Research Center for Element Strategy, International Research Frontiers Initiative, Tokyo Institute of Technology, 4259 Nagatsuta, Midori, Yokohama 226-8501, Japan.*

Abstract

Silver bismuth diselenide ($AgBiSe_2$) has much attention as an efficient thermoelectric material due to its low thermal conductivity. However, $AgBiSe_2$ exhibits multiple crystal structural transitions with temperature, and high thermoelectric performance was realized only in high-temperature cubic phase. We previously reported the stabilization of cubic phase in $AgBiSe_{2-2x}S_xTe_x$ with x = 0.6–0.8 at room temperature by high-entropy-alloy (HEA) approach. In this paper, we succeeded in stabilizing the cubic phase in $AgBiSe_{2-2x}S_xTe_x$ with x = 0–0.6 by ice-quenching method, and investigated the HE effect on the thermoelectric properties below room temperature to avoid the emergence of hexagonal phase above room temperature. Cubic $AgBiSe_{2-2x}S_xTe_x$ exhibited n-type conductivity from 300 K to 10 K. The increase in electrical conductivity is due to a combined effect of increased charge density and electron mobility, depending on the sample. It is evident that the charge carrier density strongly increases in the x = 0.4 sample while the mobility remains roughly the same compared to x = 0.0 sample. In the x = 0.2 and 0.6 samples, the electronic conductivity increases primarily due to enhanced mobility. The S and Te substitutions induced the variation of band structure, resulting in the carrier mobility enhancement. Furthermore, thermal conductivity showed reduction tendency with increasing the amount of S and Te due to enhancement of phonon scattering. Simultaneous electronic conductivity increase and thermal conductivity reduction resulted in the systematic improvement of the *ZT* values for HE-type cubic $AgBiSe_{2-2x}S_xTe_x$.

*Corresponding author: Aichi Yamashita

E-mail: aichi@tmu.ac.jp

Introduction

The thermoelectric generators can play an important role in a sustainable energy solution since they can directly convert heat into electricity. Thermoelectric energy conversion efficiency is defined as figure of merit ZT; $ZT = S^2T/\rho\kappa_{tot}$, where S is Seebeck coefficient, T is absolute temperature, ρ is electrical resistivity, and κ_{tot} is total thermal conductivity, respectively. The κ_{tot} is the summation of lattice (κ_{lat}) and electronic (κ_{ele}) contributions. The term of S^2/ρ, called as power factor (PF), can be maximized by carier concentration and band tuning. Therefore, high-performance thermoelectric materials require high PF and low κ_{tot}, as shown in the formula of ZT.[1]

Recently, silver bismuth diselenide ($AgBiSe_2$) has attracted much interest as a high-performance thermoelectric material due to its intrinsically low $\kappa_{tot} < 1$ $Wm^{-1}K^{-1}$ at room temperature.[2–13] Both n-type and p-type thermoelectric properties of $AgBiSe_2$ were reported. The difference in polarity of $AgBiSe_2$ is due to the defect of Se.[8] Nb-doped[3] and Cl-doped[4] $AgBiSe_2$ bulks achieved high ZT of 1 and 0.9, respectively. The remarkable characteristic of $AgBiSe_2$ is structural phase transitions with temperature, as shown in Fig. 1. It crystallizes in a hexagonal $P\bar{3}m1$ (#164) space group at room temperature, a rhombohedral $R\bar{3}m$ (#166) space group around 490 K, and a cubic $Fm\bar{3}m$ (#225) space group above 590 K. However, this complicated crystal structural transition would be a drawback for module application due to the difference in crystal structure between low-temperature and high-temperature sides. This transition issue was solved by our previous work using the concept of high-entropy-alloys (HEAs).[13] HEAs are typically defined as − (a) alloys containing five or more elements with a concentration between 5 and 35%, (b) 1.5R or more mixing entropy ΔS_{mix}, calculated by $\Delta S_{mix} = -R\Sigma_i c_i \ln c_i$, where c_i and R are the compositional ratio and the gas constant, respectively.[14,15] HEAs introduce a new path of developing advanced materials with unique properties such as severe lattice-distortion effect, fatigue strength, and sluggish diffusion effect. The HEAs have been developed for “metal alloys”; on the other hand, many high-entropy-type (HE-type) compounds, for which the HEAs concept is extended, have been reported recently. For instance, new HE-type layered compounds and NaCl-type metal chalcogenides as superconductors and thermoelectric

materials have been reported.[13,16–24] Focused on thermoelectric materials, HE-type compounds are expected to − (a) the stabilization of solid solution phases by decreasing Gibbs free energy with an increase in the entropy, (b) the reduction of the κ_{lat} by enhancing lattice disorder.[25] Recently we have reported new HE-type $AgBiSe_{2-2x}S_xTe_x$ with ultra-low κ_{lat} and maximum ZT value of 0.9 without optimizing carrier concentration.[26] The cubic phase was successfully stabilized at room temperature with above $x = 0.6$. According to the analysis of κ_{lat} in the hexagonal phase, the point defects scattering (PDS) model estimated with the contribution of mass and strain contrast indicates the lattice disorder and/or strain by S and Te substitution fostered the phonon scattering and contributed to the decrease of κ_{lat}. However, the S and Te substitution effects on the thermoelectric properties including the mechanism of the decrease of κ_{lat} in the cubic phase could not be discussed in whole x amount due to the appearance of the impurity phase at high temperature and incompletely stabilized cubic phase between $x = 0$-0.5 at room temperature. In the present work, we successfully stabilized the cubic phase of HE-type $AgBiSe_{2-2x}S_xTe_x$ with $x = 0$-0.6 by conducting the ice-quenching at the enough high temperature for single phase of cubic structure,[26] and investigated the S and Te substitution effects on the thermoelectric properties below room temperature.

Experimental

Polycrystalline samples of $AgBiSe_{2-2x}S_xTe_x$ with x = 0, 0.2, 0.4, 0.6 were prepared by melting method using elemental grains of Ag (99.99%, Kojundo Kagaku), Bi (99.999%, Kojundo Kagaku), Se (99.999%, Kojundo Kagaku), S (99.9999%, Kojundo Kagaku), and Te (99.999%, Kojundo Kagaku). The stoichiometric ratio of grains was annealed in an evacuated quartz tube at 1,000℃ for 15 h, and then the obtained powders were pelletized and heated at 500℃ for 20 h. Hot-press treatment was performed in order to densify the obtained compounds using graphite dies at 500℃ for 30 min under a uniaxial pressure of 60 MPa. Samples in the form of rectangular solids (typically a 1.5-mm-width, 2.5-mm-depth, 8.0-mm-hight) were cut from the cylinders using a diamond saw for electrical and thermal transport property measurements. The samples were placed in the evacuated quartz tube and heated at 450℃, which all samples become cubic phase, for 5 h. Then ice-quench treatment was performed to obtain the single phase of cubic structure. Relative density of all samples was beyond 90%, and there was no large difference in the relative density between the as-annealed and ice-quenched samples.

The actual composition was analyzed by energy-dispersive X-ray spectroscopy (EDX) on a TM-3030 (Hitachi Hightech) equipped with an EDX-SwiftED analyzer (Oxford). The phase purity and crystal structure were examined by powder X-ray diffraction (XRD), using Miniflex-600 (RIGAKU) with CuK_α radiation in Bragg-Brentano θ-2θ method with a high-resolution semiconductor detector/tex-Ultra at room temperature. The crystal structure parameters were refined using the Rietveld method using a RIETAN-FP software,[27] and crystal structures were visualized using VESTA software.[28]

Temperature dependence of electrical resistivity (ρ), Seebeck coefficient (S), and total thermal conductivity (κ_{tot}) were measured on the samples of $AgBiSe_{2-2x}S_xTe_x$ with x = 0, 0.2, 0.4, 0.6 from room temperature down to 10 K. The ρ was measured using the four-probe method with the electrical resistivity measurement option of Magnetic Property Measurement System (MPMS3, Quantum Design). A Thermal Transport Option (TTO) of Physical Property Measurement System (PPMS,

Quantum Design) was used for the κ_{tot} and the S measurements with the two-probe method. The Hall resistivity was measured with PPMS under magnetic field up to 5 T to examine the Hall coefficient R_H.

Sound velocity measurement was performed using 1077DATA (KARL DEUTSCH) for longitudinal v_{long} and transverse sound velocity v_{trans}. The Grüneisen parameter γ, Poisson ratio v_P, and mean sound velocity v_{mean} were calculated by following equations.[29]

$$\gamma = \frac{3}{2}\left(\frac{1+\nu_P}{2-3\nu_P}\right)$$

$$\nu_P = \left(1-2\left(\frac{v_{trans}}{v_{long}}\right)^2\right)\Big/\left(2-2\left(\frac{v_{trans}}{v_{long}}\right)^2\right)$$

The Debye temperature Θ_D can be written using v_{mean}, Dirac's constant $\hbar$, Boltzmann constant k_B, and volume per atom Ω.[30,31]

$$\Theta_D = \frac{\hbar}{k_B}\left(\frac{6\pi^2}{\Omega}\right)^{1/3}\cdot v_{mean}$$

$$v_{mean}{}^3 = \frac{3}{v_{long}{}^{-3} + 2v_{trans}{}^{-3}}$$

Point defect scattering model for alloy phase can assess the lattice thermal conductivity κ_{lat} using following equations.[5,6,32–35]

$$\frac{\kappa_{lat,alloy}}{\kappa_{lat,pure}} = \frac{\arctan(u)}{u}$$

The $\kappa_{lat,alloy}$ is the lattice thermal conductivity of a disordered alloy, and the $\kappa_{lat,pure}$ is the lattice thermal conductivity of a pure crystal without disorder. The disorder scaling factor u can be written using the Θ_D, the Ω, the v_{mean}, and the scattering parameter Γ.

$$u^2 = \frac{\pi\Theta_D\Omega}{2\hbar v_{mean}}\kappa_{lat,pure}\Gamma$$

The Γ is the summation of mass contribution Γ_M and strain contribution Γ_S.

$$\Gamma_M = \frac{\sum_{i=1}^{n} c_i\left(\frac{\bar{M}_i}{\bar{\bar{M}}}\right)^2 \sum_k f_i^k\left(1-\frac{M_i^k}{\bar{M}_i}\right)^2}{\left(\sum_{i=1}^{n} c_i\right)}$$

$$\Gamma_{\mathrm{S}} = \frac{\sum_{i=1}^{n} c_i \varepsilon_i \left(\frac{\bar{M}_i}{\bar{\bar{M}}}\right)^2 \sum_k f_i^k \left(1 - \frac{r_i^k}{\bar{r}_i}\right)^2}{\left(\sum_{i=1}^{n} c_i\right)}$$

$\bar{\bar{M}}$ is the average mass of compound, c_i is relative degeneracies of ith sublatt $\bar{M}_i$ and $\bar{r}_i$ are average mass and average atomic radius of ith sublattice, f_i^k is fractional occupation of kth atom of the ith sublattice, M_i^k and r_i^k are mass and atomic radius of kth atom of the ith, respectively. ε_i is the elastic parameter and regarded as a phenomenological adjustable parameter.[35]

Results and discussion

Structural characterization

Figure 2 (a) shows the room-temperature powder XRD patterns for $AgBiSe_{2-2x}S_xTe_x$ with x = 0.0–0.6 before and after quenching. All diffraction peaks for quenched samples were indexed by the rock-salt type structure (space group: $Fm\bar{3}m$, #225) which is well known as the typical high-temperature phase of $AgBiSe_2$,[2–6,8–13] indicating the successful stabilization of cubic phase without impurities at room temperature. The diffraction peaks for x = 0.0–0.4 before quenching showed the hexagonal structure. While the diffraction peaks for x = 0.6 before quenching were attributed to the rock-salt type structure, the peaks become sharper after quenching, indicating the crystallinity is much improved in the quenched sample. Rietveld refinement was performed to estimate the lattice constant and the volume of unit cell. The results of Rietveld refinement are shown in Fig. S1, and the value of lattice constant and volume are tabulated in Table 1. Fig. 2 (b) shows the relation between x of $AgBiSe_{2-2x}S_xTe_x$ and the lattice constant a. The lattice constant a systematically increased with x, and the behavior corresponds to the increase in the average ionic radius of chalcogenide sites with the equimolar ratio of S (0.184 nm, coordination number of 6) and Te (0.221 nm, coordination number of 6).

To assess the sample homogeneity, SEM imaging and EDX mapping were performed. No secondary phase was found in the SEM images (Fig. S2), and also EDX mapping (Fig. S3) revealed that there was no compositional inhomogeneity in all samples. An actual chemical composition, and mixing entropy (ΔS_{mix}) are summarized in Table 1. The actual chemical composition was estimated using the EDX, and the estimated values were almost the same as the nominal compositions, even though tiny deficiencies of chalcogenides were found. The ΔS_{mix} was estimated by the following equations.[16] The value of ΔS_{mix} at ith crystallographically independent (CI) site is given by

$$\Delta S^{i}_{\mathrm{mix}} = -R \sum_{j=1}^{N} x_j \ln x_j$$

where R, N, and x_j are the gas constant, the number of the component at the ith CI site, and the atomic fraction of the component, respectively. This formula is utilized to calculate the total mixing entropy

of the unit cell.

$$\Delta S_{\mathrm{mix}}(\mathrm{total}) = \sum_{i=1}^{n} \Delta S_{\mathrm{mix}}^{i}$$

where n is the number of the CI sites in the unit cell. According to the value ΔS_{mix} in Table 1, the samples of x = 0.4 and 0.6 can be attributed as HE-type compounds.

Electrical transport properties

The ρ of quenched $AgBiSe_{2-2x}S_xTe_x$ samples is shown in Fig. 3. The magnitude of ρ at room temperature ranged from 52 to 442 mΩcm. Systematic decrease in ρ was observed with increasing x. The temperature dependence of ρ showed different behavior from both the typical semiconductors and the previously reported hexagonal structure of $AgBiSe_2$.[3] It can be divided into following three regimes (i– iii) similar to the $(Bi, Sb)_2(Te, Se)_3$:[36,37]

(i) *Activated regime.* In the temperature range from around 100 K to 300 K, the ρ can be fitted with the Arrhenius law,

$$\rho \sim \exp(\Delta / k_{\mathrm{B}} T)$$

where Δ is the activation energy, k_{B} is the Boltzmann constant. Fig. 3(b) shows the Arrhenius plot of the data with linear fittings (solid line) to estimate Δ. In Table 1, Δ has a negative correlation with x (Fig. S4), indicating that the energy gap between the conduction band and donor level probably becomes narrower because quenched $AgBiSe_{2-2x}S_xTe_x$ samples show n-type conductivity by Hall measurement.

(ii) *Variable-range hopping (VRH) regime.* In the temperature range from ~80 K to ~100 K, the ρ can be described by Mott's 3D-VRH behavior,[38]

$$\rho \sim \exp\left[(T_0/T)^{1/4}\right]$$

where T_0 is a constant that depends on the density of state at the Fermi level E_{F}, and it is an important parameter for the extent of localization in a disordered electrical system. This hopping conduction occurs due to localized states in a narrow band near the E_{F}. The linear fittings (dashed line) of VRH

behavior are shown in Fig. 3(c). The T_0 value of x = 0.0, 0.2, 0.4, 0.6 is 7.3×10^7 K, 4.0×10^7 K, 2.4×10^7 K, and 3.1×10^7 K, respectively. It shows a reduction tendency to the x amount. Therefore, increasing the amount of S and Te induces suppression of electrons localized near E_F level. This result is consistent with the ρ behavior below the temperature of this region. The temperature range in which VRH behavior appears overlapped with the activated temperature range. The distinction between the two transport mechanisms depends on the sample's disorder level as discussed in the previous paper.[37]

(iii) *Saturation regime.* Below the VRH temperature range, the ρ tended to saturate, rather than to diverge as expected for intrinsic semiconductors. This saturation behavior implies that some extended states and two or more transport channels exist at E_F in the zero-temperature limit, moreover, chemical potential is pinned to these states.[37] Antisites between Ag, Bi cation and S, Se, Te anion are assumed as the factor of the existing these states. In Bi_2Se_3, the antisites create some shallow donor or acceptor levels;[39–41] hence, antisite should be the reason for this saturation behavior. To reveal the origin of this phenomenon, further information from the experiments, which can observe electronic defect states, such as scanning tunnel microscopy (STM) or current imaging tunneling spectroscopy (CITS).[39–41]

Figure 4(a) shows the temperature dependence of Hall carrier concentration n_H. In quenched $AgBiSe_2$, n_H gradually decreases with decreasing temperature and saturates below around 75 K, indicating Hall carrier concentration is almost constant in the saturation regime. The temperature dependence of n_H for other samples exhibited the same behavior, although it was not able to be measured below 50 K because of difficulty in the measurement of reliable Hall voltage. Temperature dependence of Hall mobility μ_H is shown in Fig. 4(b). The μ_H of almost all samples showed constant trends with decreasing temperature while activated regime. In VRH conduction, its constituent states are far away from each other, and their spatial distribution can be considered uncorrelated.[38] Hence, this μ_H behavior should be the effect of hopping conduction or some transport channels. This kind of behavior was observed in Ni-doped $CoSb_3$ which has VRH conduction in low temperature.[42] The increasing ρ with increasing x at room temperature is due to a combined effect of increasing charge n_H

and μ_H, depending on the samples. The $x = 0.4$ sample showed larger n_H and the same μ_H as the $x = 0.0$ sample, indicating that the low ρ of $x = 0.4$ compared to $x = 0.0$ is due to increasing n_H. On the other hand, the $x = 0.2$ and 0.6 samples showed the same n_H and larger μ_H as the $x = 0.0$ sample. Hence low ρ of $x = 0.2$ and 0.6 compared to $x = 0.0$ is caused by increasing μ_H.

Fig. 5(a) shows the temperature dependence of S. Around room temperature, the absolute value of S systematically decreases with increasing the amount of x. The absolute values of S slightly decreased when the temperature was reduced to ~200 K, and slightly increased until the range of 50–100 K. Finally, they dramatically decreased and became close to zero. The temperature region of S behavior corresponds to that of VRH or ρ saturation, and it implies the localized states or pinned extended states. This S behavior is similar to Ni-doped $CoSb_3$ behavior,[42] where the S vanishing is explained by the effect of the impurity band from Ni. The S behavior around room temperature corresponds to the behavior of the ρ. However, n_H contribution is less discussed above. The Pisarenko plot at 275 K is shown in Fig. 5(b). Note that the data points tend to be scattered for κ_{tot} with large error bar at around the room temperature region (Fig. S5). Hence, we selected the κ_{tot} value at 275 K which has smaller scattering of data points for all samples and closer to the sound velocity measurement temperature. They did not follow the SPB model trend, indicating that the reason for decreasing the absolute value of S should be band flattening or multi-band effect.[43,44] This result indicates that increasing μ_H with increasing x is due to the band structure modification by S and Te substitutions.

Thermal transport properties

The κ_{tot}, κ_{lat}, and κ_{ele} are shown in Fig 6(a), (b), and Fig. S5, respectively. The κ_{ele} is directly estimated using Wiedemann-Franz law: $\kappa_{ele} = LT/\rho$, where L is Lorenz number which is expressed by $L = 1.5 + \exp(-|S|/116)$ (where L is in 10^{-8} and S in μV/K).[45] The κ_{lat} is obtained by subtracting κ_{ele} from κ_{tot}. The κ_{tot} for $x = 0$ shows weak temperature dependence up to ~100 K, and largely decreased below ~100 K. Finally, κ_{tot} suddenly increased around 20 K. Around the room temperature and 20 K

regions, measurement was not stable and they have large error bar as shown in Fig. S6. The ρ and S showed unexpected behaviors possibly due to some extended states near E_F, which are also discussed in the literature by J. S. Dyck *et al.*[42]; therefore, κ_{tot} should be also affected by the aforementioned matter in the case of ~20 K region. Other samples show similar behavior and κ_{lat} almost the same, indicating that the contribution of the κ_{tot} is dominant by κ_{lat}. The κ_{lat} is expressed as $\kappa_{lat} = \frac{1}{3}C_v v_{mean} l$, where C_v is specific heat per unit cell, v_{mean} is avarage sound velocity, and l is the mean free path of phonons. According to the equation, increase in the C_v raises the κ_{lat} until around one-third of Debye temperature, and κ_{lat} almost saturates above that temperature. In general, κ_{lat} has a peak around that temperature due to the decreasing l which is caused by phonon-phonon Umklapp scattering.[46] However, the quenched $AgBiSe_{2-2x}S_xTe_x$ samples did not show the peak possibly due to the shortening of l against the temperature by severe phonon scattering systems.[47] Here, the l value of x =0.0 can be estimated using aforementioned formula of $\kappa_{lat} = \frac{1}{3}C_v v_{mean} l$. The κ_{lat} is 0.90 W/mK. The C_v is calculated by $\rho_s C_p$ where ρ_s and C_p are the sample density (7.74 g/cm^3) and specific heat under constant pressure (0.21 J/gK.), respectively.[48] C_p is estimated using the Dulong-Petit model ($C_p = 3R$). The v_{mean} of 1636.2 ms^{-1} was obtained from longitudinal sound velocity of 2888.9 ms^{-1} and transversal sound velocity of 1459.4 ms^{-1}. Finally, $l \sim 1.0$ nm was obtained. Considering this short l in the pristine sample, S and Te substitutions should decrease the l rather than x = 0.0. The κ_{lat} around room temperature almost systematically decreases with increasing x. Here, point defect scattering (PDS) model fitting was performed to assess the magnitude of the substitution effect for κ_{lat}, and the result at 275 K is shown in Fig. 6(c). This model can evaluate the κ_{lat} of the contribution of mass and strain contrast. The κ_{lat} and mean sound velocity v_{mean} of the pristine sample is required for this model. The κ_{lat} of 0.90 W/mK and the v_{mean} of 1636.2 ms^{-1} were utilized to perform the PDS model. The ε of 5 gives good fitting for the trend of quenched $AgBiSe_{2-2x}S_xTe_x$. No deviation between the mass contribution and mass and strain contribution in Fig. 6(c) suggests that the mass contribution dominates in this cubic system. The ε of the hexagonal $AgBiSe_{2-2x}S_xTe_x$ is 32.5,[26] showing that the contribution fraction of mass and strain

is largely different. This difference should be due to the difference in anharmonicity. The Grüneisen parameter of the hexagonal $AgBiSe_2$ was estimated as 1.68[13], while that of the cubic $AgBiSe_2$ was 1.97, indicating the high anharmonicity nature of the cubic structure of $AgBiSe_2$ system. Moreover, the atomic bond length of the cubic phase is more fluctuated than that of the hexagonal phase for $AgBiSe_2$.[7] Hence, the pristine cubic sample already has a large strain indicating that the contribution of substitution of S and Te for strain should be small.

The power factor PF of quenched $AgBiSe_{2-2x}S_xTe_x$ is shown in Fig. 7(a). The PF for $x = 0$ was 0.54 $\mu Wcm^{-1}K^{-2}$ at room temperature and decreased with the temperature. The maximum PF among the obtained samples were 1.27 $\mu Wcm^{-1}K^{-2}$ for $x = 0.6$ at room temperature. Although PF for $x = 0.4$ and 0.6 showed almost the same values of PF, it tended to increase with increase in the x amount.

Fig. 7(b) shows the ZT of quenched $AgBiSe_{2-2x}S_xTe_x$. The ZT values systematically increased with x amount, indicating that the simultaneous substitution of Se site by S and Te improved the ZT values due to the improvement of both electrical and thermal properties. The maximum ZT reached 0.05 with $x = 0.6$ at room temperature.

Conclusion

In summary, we successfully stabilize the high-temperature cubic phase in $AgBiSe_{2-2x}S_xTe_x$ with $x = 0$–0.6 at room temperature by ice-quench technique and investigated the HE effects on the thermoelectric properties of the cubic phase below room temperature to avoid the decomposition of cubic phase to hexagonal phase. Around room temperature, systematic change of electrical transport properties was observed and it was discussed using SPB model. In consequence, it was explained by the variation of band structure. In lower temperature regions, the ρ showed 3D-VRH and saturated behavior possibly due to some localized states or extended states near E_F. Moreover, the vanishment of S around 50 K also could be caused by the same mechanism. The existence of some transport channels is consistent with the result of the Pisarenko plot, suggesting that the simultaneous substitution of S and Te for Se site should affect band structure. The temperature dependence of κ_{lat}

without a peak around 50 K indicates the shortening of *l* for $AgBiSe_{2-2x}S_xTe_x$, possibly due to the severe phonon scattering. Finally, the *ZT* value of 0.05 was achieved for the $x = 0.6$ sample at room temperature. Our work offered an approach to investigate the thermoelectric properties of cubic structure of $AgBiSe_{2-2x}S_xTe_x$ and we succeeded in enhancing the thermoelectric properties around room temperature.

Author Contributions

AS synthesized and characterized the mateials, and wrote the first draft of the manuscript. AY supervized the work, edited and finalized the manuscript. TK performed Sound velocity measurement and Hall coefficient measurement, edited and finalized the manuscript. YM supervised the work, edited the manuscript.

Conflicts of interest

There are no conflicts to declare.

Acknowledgements

The authors thank Hiroto Arima for his supports in experiments. This work was partially performed with Collaborative Research Project of Laboratory for Materials and Structures, Institute of Innovative Research, Tokyo Institute of Technology. A. Y. was partly supported by a Grant-in-Aid for Scientific Research (KAKENHI) (No. 22K14480), and the Asahi Glass Foundation. Y. M. was partly supported by a Grant-in-Aid for Scientific Research (KAKENHI) (No. 21H00151), JST-ERATO (No. JPMJER2201), and the Tokyo Metropolitan Government Advanced Research (No. H31-1).

Reference

1 G. J. Snyder and E. S. Toberer, *Nat. Mater.*, 2008, **7**, 105–114.
2 C. Xiao, X. Qin, J. Zhang, R. An, J. Xu, K. Li, B. Cao, J. Yang, B. Ye and Y. Xie, *J. Am. Chem. Soc.*, 2012, **134**, 18460–18466.
3 L. Pan, D. Bérardan and N. Dragoe, *J. Am. Chem. Soc.*, 2013, **135**, 4914–4917.

4 S. N. Guin, V. Srihari and K. Biswas, *J. Mater. Chem. A*, 2014, **3**, 648–655.

5 F. Böcher, S. P. Culver, J. Peilstöcker, K. S. Weldert and W. G. Zeier, *Dalton Trans.*, 2017, **46**, 3906–3914.

6 Y. Goto, A. Nishida, H. Nishiate, M. Murata, C. H. Lee, A. Miura, C. Moriyoshi, Y. Kuroiwa and Y. Mizuguchi, *Dalton Trans.*, 2018, **47**, 2575–2580.

7 T. Bernges, J. Peilstöcker, M. Dutta, S. Ohno, S. P. Culver, K. Biswas and W. G. Zeier, *Inorg. Chem.*, 2019, **58**, 9236–9245.

8 S. Li, Z. Feng, Z. Tang, F. Zhang, F. Cao, X. Liu, D. J. Singh, J. Mao, Z. Ren and Q. Zhang, *Chem. Mater.*, 2020, **32**, 3528–3536.

9 T. Zhao, H. Zhu, B. Zhang, S. Zheng, N. Li, G. Wang, G. Wang, X. Lu and X. Zhou, *Acta Mater.*, 2021, **220**, 117291.

10 H. Zhu, T. Zhao, B. Zhang, Z. An, S. Mao, G. Wang, X. Han, X. Lu, J. Zhang and X. Zhou, *Adv. Energy Mater.*, 2021, **11**, 2003304.

11 Z. Guo, Y.-K. Zhu, M. Liu, X. Dong, B. Sun, F. Guo, Q. Zhang, J. Li, W. Gao, Y. Fu, W. Cai, J. Sui and Z. Liu, *Mater. Today Phys.*, 2023, **38**, 101238.

12 L. Zhang, W. Shen, Z. Zhang, C. Fang, Q. Wang, B. Wan, L. Chen, Y. Zhang and X. Jia, *J. Materiomics*, 2024, **10**, 70–77.

13 A. Seshita, A. Yamashita, T. Fujita, T. Katase, A. Miura, Y. Nakahira, C. Moriyoshi, Y. Kuroiwa and Y. Mizuguchi, 2024.

14 J.-W. Yeh, S.-K. Chen, S.-J. Lin, J.-Y. Gan, T.-S. Chin, T.-T. Shun, C.-H. Tsau and S.-Y. Chang, *Adv. Eng. Mater.*, 2004, **6**, 299–303.

15 J.-W. Yeh, *JOM*, 2013, **65**, 1759–1771.

16 A. Yamashita, Y. Goto, A. Miura, C. Moriyoshi, Y. Kuroiwa and Y. Mizuguchi, *Mater. Res. Lett.*, 2021, **9**, 366–372.

17 R. Sogabe, Y. Goto and Y. Mizuguchi, *Appl. Phys. Express*, 2018, **11**, 053102.

18 R. Sogabe, Y. Goto, T. Abe, C. Moriyoshi, Y. Kuroiwa, A. Miura, K. Tadanaga and Y. Mizuguchi, *Solid State Commun.*, 2019, **295**, 43–49.

19 Y. Mizuguchi, *J. Phys. Soc. Jpn.*, 2019, **88**, 124708.

20 M. R. Kasem, K. Hoshi, R. Jha, M. Katsuno, A. Yamashita, Y. Goto, T. D. Matsuda, Y. Aoki and Y. Mizuguchi, *Appl. Phys. Express*, 2020, **13**, 033001.

21 Y. Shukunami, A. Yamashita, Y. Goto and Y. Mizuguchi, *Phys. C Supercond. Its Appl.*, 2020, **572**, 1353623.

22 A. Yamashita, R. Jha, Y. Goto, T. D. Matsuda, Y. Aoki and Y. Mizuguchi, *Dalton Trans.*, 2020, **49**, 9118–9122.

23 Y. Mizuguchi, Md. R. Kasem and T. D. Matsuda, *Mater. Res. Lett.*, 2021, **9**, 141–147.

24 Md. R. Kasem, A. Yamashita, Y. Goto, T. D. Matsuda and Y. Mizuguchi, *J. Mater. Sci.*, 2021, **56**, 9499–9505.

25 B. Jiang, Y. Yu, J. Cui, X. Liu, L. Xie, J. Liao, Q. Zhang, Y. Huang, S. Ning, B. Jia, B. Zhu, S. Bai,

L. Chen, S. J. Pennycook and J. He, *Science*, 2021, **371**, 830–834.
26 A. Seshita, A. Yamashita, T. Fujita, T. Katase, A. Miura, Y. Nakahira, C. Moriyoshi, Y. Kuroiwa and Y. Mizuguchi, arXiv:2404.00984, 2024.
27 F. Izumi and K. Momma, *Solid State Phenom.*, 2007, **130**, 15–20.
28 K. Momma and F. Izumi, *J. Appl. Crystallogr.*, 2011, **44**, 1272–1276.
29 D. S. Sanditov and V. N. Belomestnykh, *Tech. Phys.*, 2011, **56**, 1619–1623.
30 O. L. Anderson, *J. Phys. Chem. Solids*, 1963, **24**, 909–917.
31 A. Zevalkink, E. S. Toberer, W. G. Zeier, E. Flage-Larsen and G. J. Snyder, *Energy Environ. Sci.*, 2011, **4**, 510–518.
32 J. Yang, G. P. Meisner and L. Chen, *Appl. Phys. Lett.*, 2004, **85**, 1140–1142.
33 P. G. Klemens, *Proc. Phys. Soc. Sect. A*, 1955, **68**, 1113.
34 J. Callaway and H. C. von Baeyer, *Phys. Rev.*, 1960, **120**, 1149–1154.
35 B. Abeles, *Phys. Rev.*, 1963, **131**, 1906–1911.
36 Z. Ren, A. A. Taskin, S. Sasaki, K. Segawa and Y. Ando, *Phys. Rev. B*, 2010, **82**, 241306.
37 Z. Ren, A. A. Taskin, S. Sasaki, K. Segawa and Y. Ando, *Phys. Rev. B*, 2011, **84**, 165311.
38 B. I. Shklovskii and A. L. Efros, Springer Berlin Heidelberg, Berlin, Heidelberg, 1984, vol. 45.
39 S. Urazhdin, D. Bilc, S. H. Tessmer, S. D. Mahanti, T. Kyratsi and M. G. Kanatzidis, *Phys. Rev. B*, 2002, **66**, 161306.
40 G. Wang, X.-G. Zhu, Y.-Y. Sun, Y.-Y. Li, T. Zhang, J. Wen, X. Chen, K. He, L.-L. Wang, X.-C. Ma, J.-F. Jia, S. B. Zhang and Q.-K. Xue, *Adv. Mater.*, 2011, **23**, 2929–2932.
41 M. Lee, S. W. Cho, Y. Yi and S. Lee, *J. Alloys Compd.*, 2019, **800**, 81–87.
42 J. S. Dyck, W. Chen, J. Yang, G. P. Meisner and C. Uher, *Phys. Rev. B*, 2002, **65**, 115204.
43 A. F. May and G. J. Snyder, *Introduction to Modeling Thermoelectric Transport at High Temperatures*, CRC Press, Boca Raton, FL, USA 2012, 1–18.
44 Y. Luo, S. Hao, S. Cai, T. J. Slade, Z. Z. Luo, V. P. Dravid, C. Wolverton, Q. Yan and M. G. Kanatzidis, *J. Am. Chem. Soc.*, 2020, **142**, 15187–15198.
45 H.-S. Kim, Z. M. Gibbs, Y. Tang, H. Wang and G. J. Snyder, *APL Mater.*, 2015, **3**, 041506.
46 A. Yamashita, K. Kihou, H. Kunioka, H. Nishiate, A. Yamamoto, Y. Goto, Y. Mizuguchi, T. Iida, Y. Takano and C.-H. Lee, *J. Solid State Chem.*, 2020, **291**, 121588.
47 J. Zhang, X. Y. Qin, H. X. Xin, D. Li and C. J. Song, *J. Electron. Mater.*, 2011, **40**, 980–986.
48 J. X. Tan, J. Ding, H. Luo, O. Delaire, J. Yang, Z. Zhou, J.-L. Lan, Y.-H. Lin and C.-W. Nan, *ACS Appl. Mater. Interfaces*, 2020, **12**, 41333–41341.

Figure

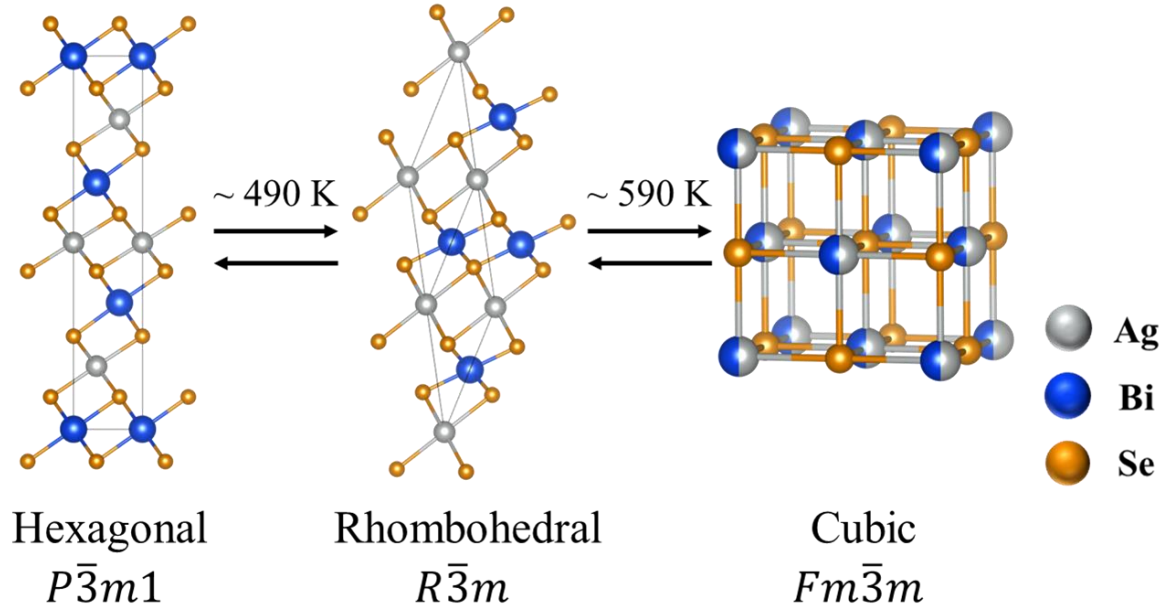

Fig. 1 Temperature dependence of crystal structure change in $AgBiSe_2$.

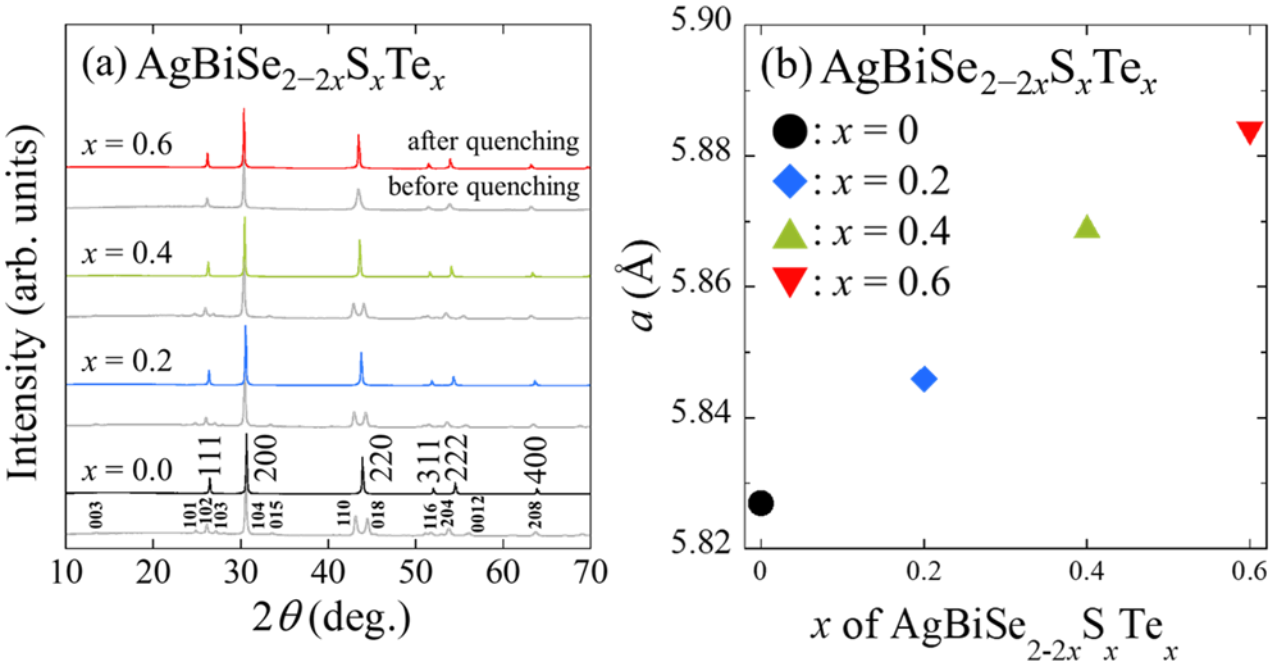

Fig. 2 (a) X-ray diffraction (XRD) patterns of quenched $AgBiSe_{2-2x}S_xTe_x$ samples at room temperature. XRD patterns of before quenching samples were also plotted below those of each quenched sample as a comparison. (b) The lattice constant of quenched $AgBiSe_{2-2x}S_xTe_x$ samples at room temperature.

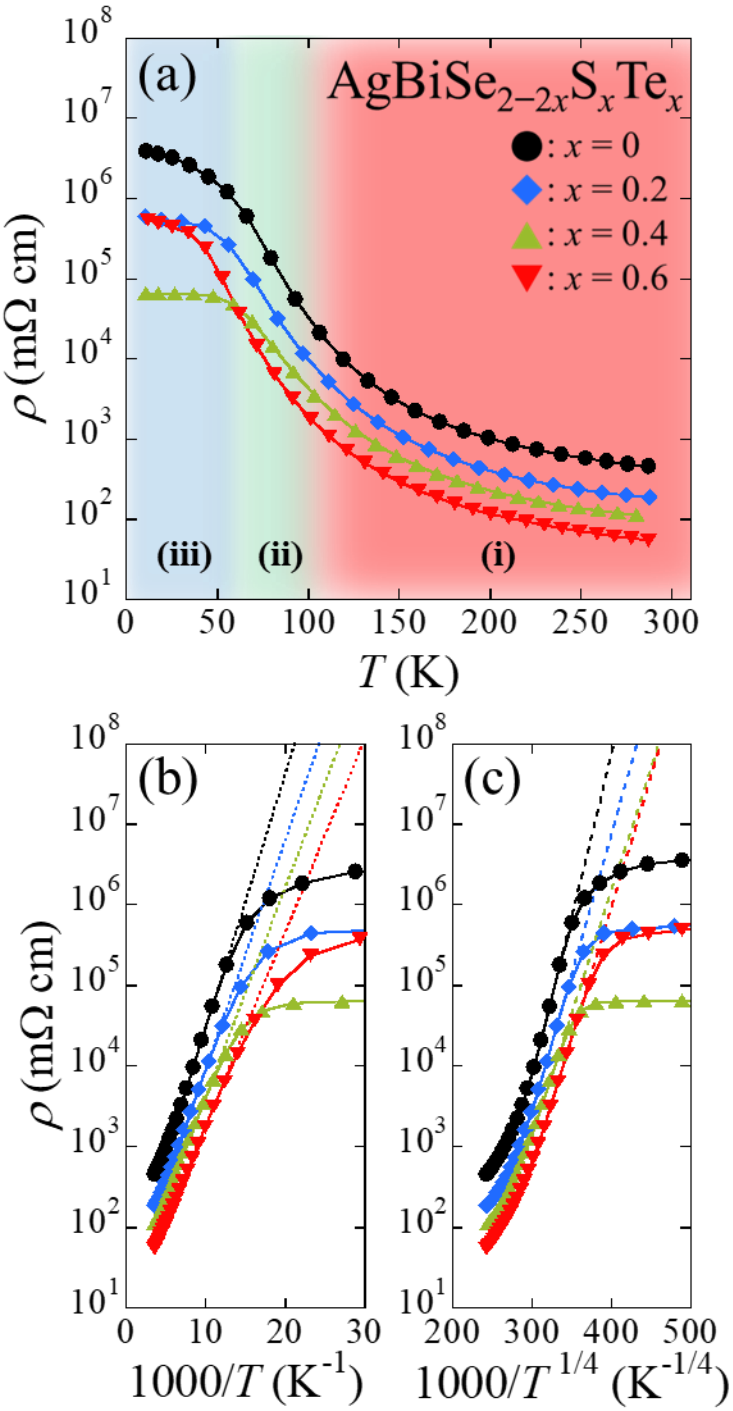

Fig. 3 Temperature (T) dependence of electrical resistivity (ρ) for quenched $AgBiSe_{2-2x}S_xTe_x$ samples. Red, green and blue regions are activated regime, variable-range hopping (VRH) regime and saturation regime, respectively. (b) and (c) are the Arrhenius plot [$\log_{10}\rho$ vs $1000/T$] and the 3D- VRH plot [$\log_{10}\rho$ vs $1000/T^{1/4}$] of electrical resistivity data, respectively. Dotted and Dashed lines represent linear fittings of the activation and VRH behaviors, respectively.

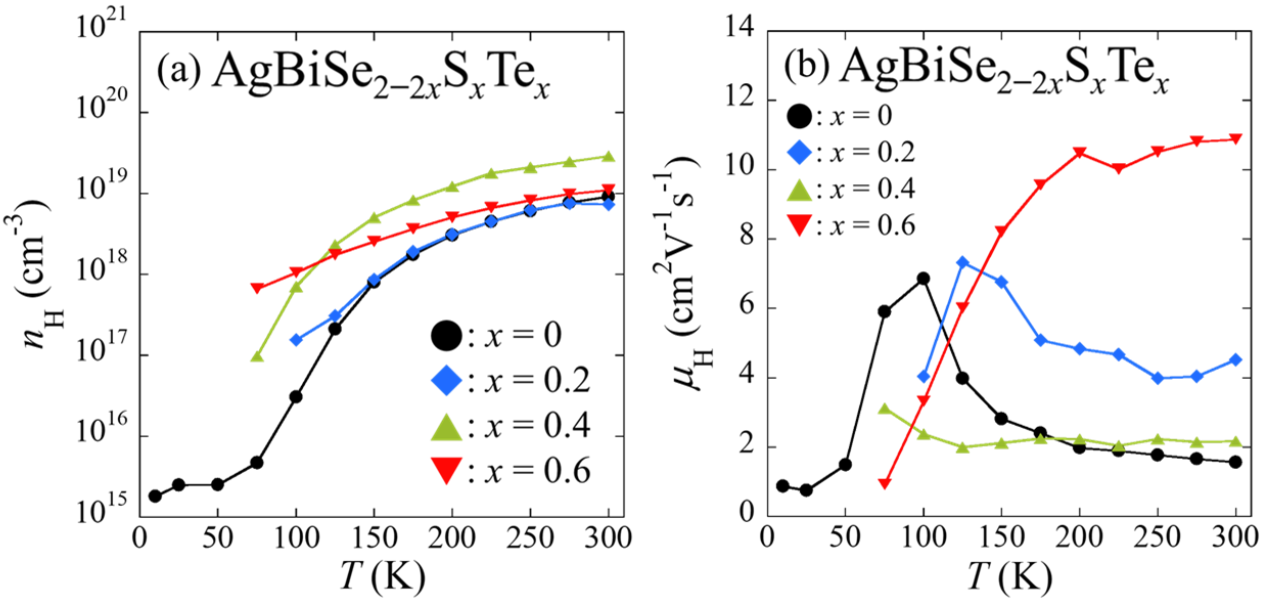

Fig. 4 Temperature (T) dependence of (a) Hall carrier concentration (n_H), and (b) Hall mobility (μ_H) for quenched $AgBiSe_{2-2x}S_xTe_x$ samples.

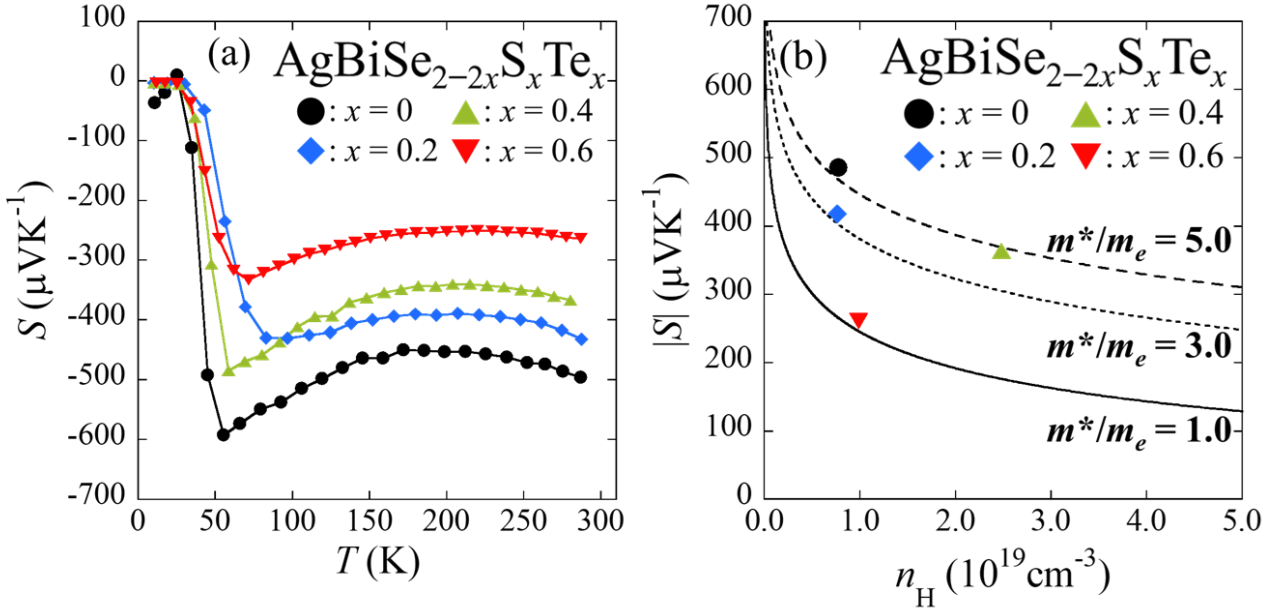

Fig. 5 Temperature (T) dependence of (a) Seebeck coefficient (S). (b) Pisarenko plots for absolute S ($|S|$) vs Hall carrier concentration (n_H) at 275 K.

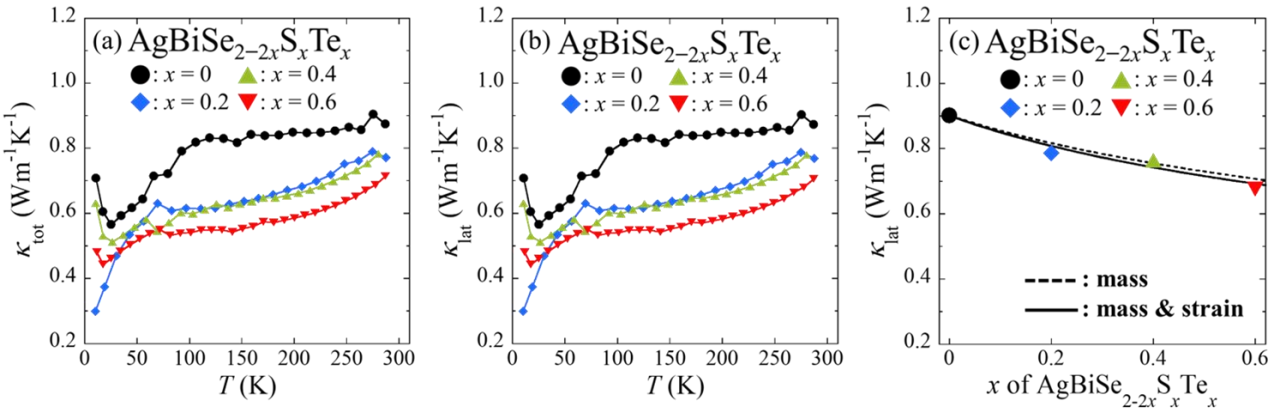

Fig. 6 Temperature dependence of (a) total thermal conductivity (κ_{tot}) and (b) lattice thermal conductivity (κ_{lat}) for quenched $AgBiSe_{2-2x}S_xTe_x$ samples. (c) PDS model fitting to κ_{lat} (color plots) at 275 K. The Dashed line shows mass contribution, and the solid line shows mass and strain contributions.

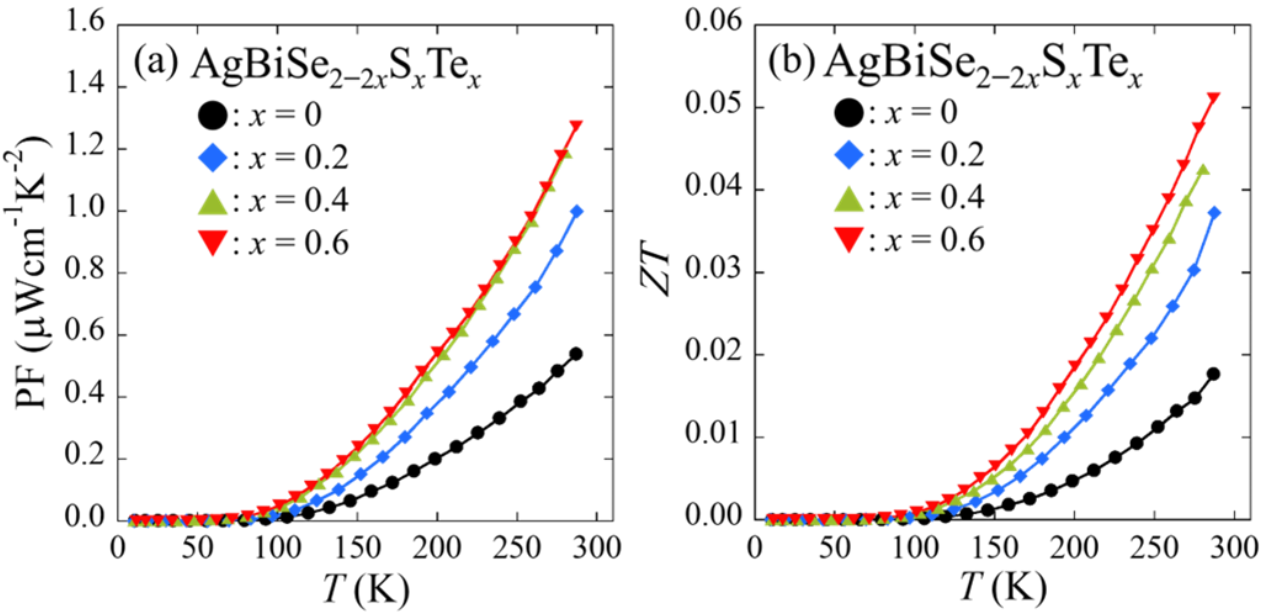

Fig. 7 Temperature dependence of (a) PF and (b) *ZT* of quenched $AgBiSe_{2-2x}S_xTe_x$ samples.

Table 1 Chemical composition, mixing entropy, lattice constant, volume, and activation energy of electrical resistivity for quenched $AgBiSe_{2-2x}S_xTe_x$ samples.

x	nominal	actual	$\Delta S_{\mathrm{mix}}/R$	a (Å)	V (Å^3)	Δ (meV)
0.0	$AgBiSe_2$	$Ag_{1.02}Bi_{1.04}Se_{1.94}$	0.693	5.8269	197.84	62.2
0.2	$AgBiSe_{1.6}S_{0.2}Te_{0.2}$	$Ag_{1.04}Bi_{1.02}Se_{1.58}S_{0.15}Te_{0.21}$	1.403	5.8459	199.78	55.9
0.4	$AgBiSe_{1.2}S_{0.4}Te_{0.4}$	$Ag_{1.04}Bi_{1.03}Se_{1.17}S_{0.36}Te_{0.40}$	1.659	5.8692	202.18	51.3
0.6	$AgBiSe_{0.8}S_{0.6}Te_{0.6}$	$Ag_{1.02}Bi_{1.03}Se_{0.80}S_{0.57}Te_{0.57}$	1.764	5.8834	203.65	47.6

Data Availability Statement

All Figures and Tables are available upon request from the authors